MDPI

Article

Enhancing Li-S Battery Performance with Porous Carbon from Hanji

Yunju Choi [1,2], Jaeyeong Lee [3], Jong-Pil Kim [1], Sei-Jin Lee [4], Euh Duck Jeong [1], Jong-Seong Bae [1,*,†] and Heon-Cheol Shin [2,*,†]

[1] Busan Center, Korea Basic Science Institute (KBSI), Busan 46742, Republic of Korea;
    yjchoi0512@kbsi.re.kr (Y.C.); jpkim@kbsi.re.kr (J.-P.K.); edjeong@kbsi.re.kr (E.D.J.)
[2] Department of Materials Science and Engineering, Pusan National University, Busan 46241, Republic of Korea
[3] Accelerator Strategy Team, KBSI, Daejeon 34133, Republic of Korea; jlee0321@kbsi.re.kr
[4] Jeonju Center, KBSI, Jeonju 54907, Republic of Korea; lsj@kbsi.re.kr
[*] Correspondence: jsbae@kbsi.re.kr (J.-S.B.); hcshin@pusan.ac.kr (H.-C.S.)
[†] These authors contributed equally to this work.

Abstract: Hanji-derived porous carbon has been developed and utilized as a cathode material for Li-S batteries, demonstrating exceptional electrochemical performance and stability. The unique porous structure and high surface area of Hanji-based carbon enhanced S utilization and significantly improved the overall efficiency of the battery. The material exhibited excellent electrical conductivity and structural stability, effectively addressing the major challenges of Li-S batteries, such as the polysulfide shuttle effect and active material loss. In addition, flake carbon-coated separators (FCCSs) were integrated into Li-S cells to further enhance their performance, achieving a high initial specific capacity of approximately 1200 mAh/g and maintaining a capacity of 620 mAh/g after 100 cycles. In contrast, cells with conventional polypropylene separators exhibited lower initial capacities (946 mAh/g), which decreased to 366 mAh/g after 100 cycles. FCCSs also demonstrated superior capacity retention and stability under varying charge–discharge rates, maintaining a capacity of 200 mAh/g at 3 C and recovering to 730 mAh/g when the rate was 0.1 C. This study provides valuable insights into the development of sustainable and efficient Li-S battery systems, with Hanji-based carbon and FCCSs emerging as promising components for commercial applications.

check for updates

1. Introduction

Li-S batteries are measured to be a promising next-generation battery technology capable of addressing the low energy density limitations of currently commercialized Li ion batteries [1,2]. Significant research and development efforts are underway to advance this technology [3]. When S is used as the cathode material, Li-S batteries show a high theoretical specific capacity of 1675 mAh/g and an energy density of 2600 Wh/kg [4]. S is an abundant and low-cost material that is often produced as an industrial byproduct of desulfurization during crude oil refinement. Li-S batteries generate electrical energy during discharge through a reaction between Li and S, forming lithium sulfide (Li_2S), with the reverse reaction occurring during charging [5,6]. During this process, S in its S_8 form receives Li ions and electrons, undergoing reduction and ring-opening reactions [7]. Intermediate lithium polysulfides (Li_2S_x, where x = 1–8) are sequentially reduced, shortening their chain length and releasing energy as Li_2S is formed [8,9].
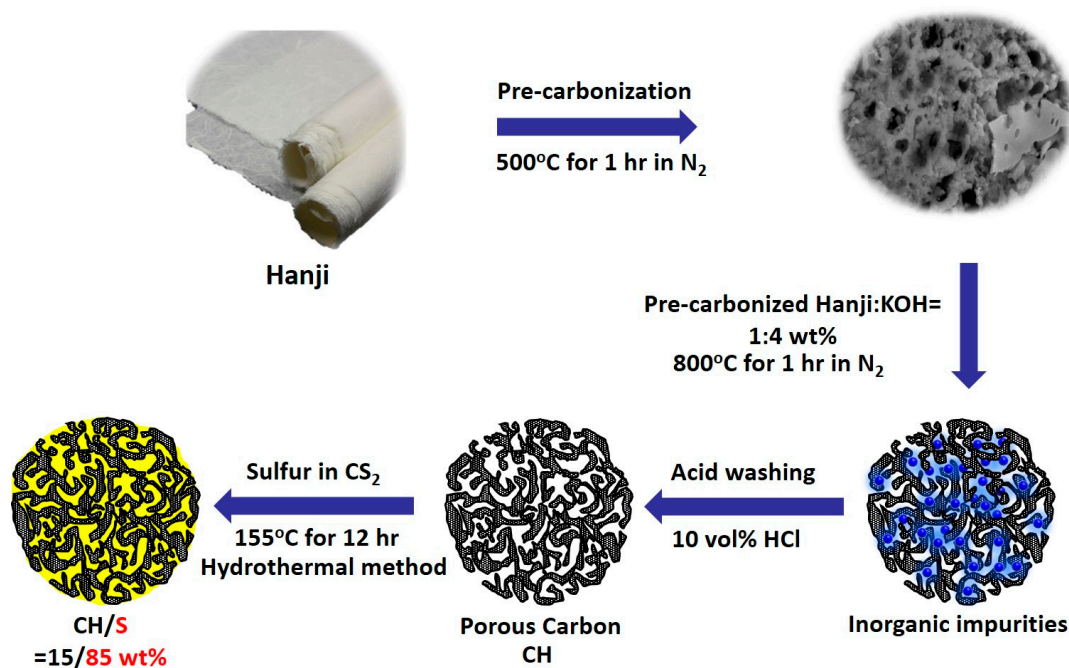
However, Li-S batteries face several challenges [10], including polysulfide dissolution, the loss of active S in the cathode, poor conductivity, reduced coulomb efficiency, and capacity loss. Enhancing the electrochemical efficiency of Li-S batteries requires the close interaction of sulfur with conductive materials, which can be grouped into several categories. Commonly used carbon materials, such as amorphous carbon [11] and carbon black [12], are valued for their widespread availability and good conductivity. Similarly, graphene-based materials, like graphene oxide [13], and conductive polymer coatings [14] exhibit excellent conductivity and chemical durability. Porous carbon structures—ranging from macroporous to microporous forms [15]—provide large surface areas for sulfur containment, while nanostructured carbons, including carbon nanofibers and nanotubes [16], enhance ion and electron transport. Moreover, graphitized carbon frameworks [17] are recognized for their structural stability and high conductivity. Recently, increasing attention has been directed toward the development of sustainable active carbons derived from biomass, which not only tackle issues such as polysulfide shuttling but also improve overall battery performance. In recent years, research has focused on incorporating active carbon derived from biomass sources, such as potatoes [18], eggshells [19], banana peels [20], bamboo leaves [21], soybeans [22], corncobs [23], pomelo peels [24], shaddock peels [25]. Our group has also reported Li-S battery research using thiourea-based porous carbon and calcium citrate [26], as well as biomass-derived porous carbon from garlic peels [27].

Hanji is a traditional paper produced from the bast fibers of mulberry trees. In this study, Hanji was selected as the carbon precursor for Li-S batteries to enhance their electrical conductivity for the following reasons. First, Hanji possesses a unique fibrous structure that retains excellent porosity and mechanical stability even after carbonization. These structural properties make it highly suitable for improving electrochemical performance. Second, Hanji is an environmentally friendly and sustainable material, and the motivation to recycle waste paper was also a key factor in its selection. This study aimed to reduce its environmental impact while obtaining a high-performance carbon material, making Hanji an ideal choice for the research. CH-S was manufactured by heating a mixture of sulfur and Hanji. The electrochemical properties of the CH-S cathodes in Li-S batteries were evaluated through charge–discharge cycling tests, C-rate assessments, and impedance measurements. Additionally, a separator coated with flake carbon was incorporated into the Li-S battery cell to investigate the extent of the increase in battery capacity.

2. Experiment

2.1. Preparation of Carbonized Hanji (CH) and Carbonized Hanji–Thiourea(CH/TU)

Hanji is a Korean paper made from mulberry trees using traditional methods. Commercially available Hanji products readily obtainable in the market were utilized in this study. As shown in Figure 1, this study produced carbonized Hanji. The paper was rinsed with deionized water to eliminate impurities and surface particles, followed by a drying process. Subsequently, two pre-treatment methods (pre-carbonization and hydrothermal) were performed. The Hanji was pre-carbonized at 500 °C for 1 h in a cylindrical furnace under a nitrogen flow of 200 cm^3/min. The pre-carbonized material was subsequently activated by combining it with an aqueous potassium hydroxide solution (45 wt.% in H_2O, Sigma Aldrich, St. Louis, MI, USA) at a 1:2 weight ratio, followed by heating at 800 °C for 1 h in the same cylindrical furnace. Finally, residual impurities were removed by washing the material with 1.0 M hydrochloric acid (ACS reagent, Aldrich, St. Louis, MI, USA), followed by multiple rinses with high-purity deionized water until a neutral pH was achieved. In the case of CH/TU, thiourea (TU) was added to the pre-carbonized Hanji, followed by a heat treatment and washing process conducted in the same manner as previously described, resulting in the production of CH/TU.

Figure 1. Diagrammatic representation of the process for creating the carbonized Hanji/sulfur (CH/S) composite.

2.2. Preparation of CH-S and CH/TU-S Composites

To incorporate the S, the CH and CH/TU materials were synthesized through wet impregnation using a S solution. S powder (reagent grade, Aldrich) was solvated in carbon disulfide (CS_2, ACS reagent, Aldrich) and the resulting yellow mixture was used to impregnate the CH and CH/TU samples. The impregnated samples were initially dried in a fume hood at 60 °C for several hours. Subsequently, they were placed in a Teflon-lined autoclave vessel and heated in air at 150 °C for 12 h in a box furnace.

2.3. Preparation of Flake Carbon-Coated Separator (FCCS)

A slurry was arranged by mixing flake graphite (0.2 g) with melted polyvinylidene fluoride (PVdF) in N-methyl-2-pyrrolidone, maintaining a weight ratio of 9:1 between the graphite and PVdF. This slurry was then applied onto a commercial polypropylene (PP) membrane separator (Celgard 2400, Charlotte, NC, USA, 25 μm thickness). After being air-dried at room temperature for 1 h, the coated separator was then additionally dried in a vacuum oven at 50 °C for 6 h. The dehydrated film was subsequently compressed by rolling, fabricating the flake carbon-coated separator (FCCS).

2.4. Material Characterization

The surface areas and pore sizes of the porous carbon composites were evaluated using the Brunauer–Emmett–Teller (BET) method and the Barrett–Joyner–Halenda (BJH) technique. X-ray diffraction (XRD) analysis was carried out with a PANalytical Malvern system (40 kV, 15 mA), utilizing Cu Kα radiation (λ = 1.5406 Å) to acquire diffraction patterns. The procedure involved scanning from 10° to 80° at a scanning rate of 3° per minute to confirm the crystalline structure of the samples prepared. Raman spectroscopy was performed at room temperature with a 532 nm laser operating at 3.0 mW power (Xper-RamII, Nano Base, Seoul, Republic of Korea). Elemental valence states and surface compositions were examined through X-ray photoelectron spectroscopy (XPS, Thermo Fisher Scientific K-Alpha+, Waltham, MA, USA), which used an X-ray source (Al-Kα radiation, hν = 1486.6 eV) and an analysis area of 400 μm, along with charge compensation.

Photoelectron collection was achieved using a multichannel detector positioned at a 90° angle from the sample surface. During the analysis, the turbo-pumped chamber maintained a vacuum of 1.2×10^{-9} mbar. Analysis scans were performed using a pass energy of 200 eV with a resolution of 1 eV, and high-resolution scans were performed at a pass energy of 50 eV with a resolution of 0.1 eV. All binding potentials were referenced to the adventitious carbon (C 1 s) peak at 284.6 eV. The sulfur content in the composites was quantified using a thermogravimetric analyzer (TG, TA Q600-0825, New castle, DE, USA) under a nitrogen environment at temperatures up to 600 °C, with a heating rate of 10 °C/min. The structures of the samples were examined using scanning electron microscopy (SEM, Hitachi SU-70, Tokyo, Japan) at acceleration voltages of 30 and 200 kV. Additionally, transmission electron microscopy (TEM, JEM-2100F, JEOL, Akishima, Japan) was utilized to examine the structure and conduct elemental mapping of the cathode material at the nanoscale.

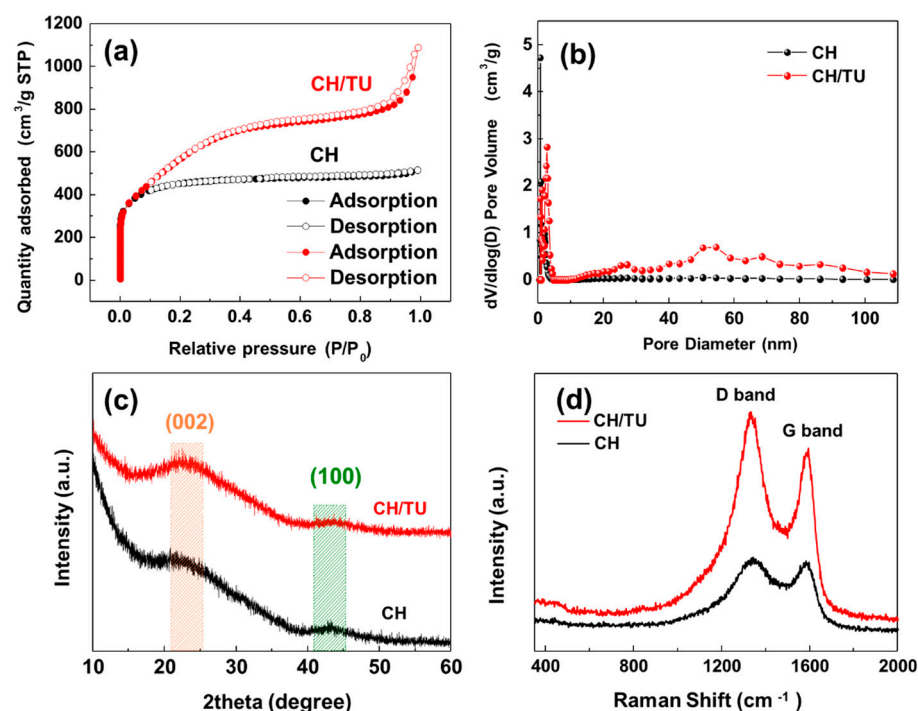*2.5. Electrochemical Measurements*

Electrochemical evaluations of the CH-S were conducted using CR2032 coin cells, which were assembled in an argon-filled glove box with lithium foil serving as the counter electrode. To prepare the working electrode, as-synthesized active CH-S, conductive Denka Black (20 wt. %), and the PVdF (Solef® 5130, Solvay, Tavaux, France, 2.5 wt. % dissolved in N-methyl-2-pyrrolidone, 10 wt. %) binder were mixed in a N-methyl-2-pyrrolidone solvent. The prepared slurry was then coated onto an aluminum foil current collector and dried at 80 °C for a duration of two hours. Composite cathodes of the CH/TU-S were fabricated with a weight ratio of active material to conductive material to PVdF binder of 70:20:10 using an identical preparation method.

The final electrode had a thickness of about 30 µm, and the active material's loading mass was roughly 1 mg cm^{-1}. A Celgard 2400 polypropylene membrane served as the separator, and 1.0 M lithium bis(trifluoromethanesulfonyl)imide and 0.4 M LiNO$_3$ in a solvent mixture of 1:1 (volume) dioxolane–dimethoxyethane served as the electrolyte. Electrochemical cycling and rate assessments were conducted within a voltage window of 1.5–2.8 V vs. Li/Li$^+$, and cyclic voltammetry was executed at a scan rate of 0.05 mV s^{-1} utilizing a galvanostatic/potentiostatic system (WonATech Co., Ltd., Seoul, Republic of Korea). Additionally, Electrochemical Impedance Spectroscopy (EIS) assessments were conducted with a ZIVE SP2 analyzer (WonATech Co., Ltd., Republic of Korea), spanning frequencies between 1 MHz and 10 mHz and applying an AC amplitude of 10 mV.

3. Results and Discussion

As displayed in Figure 2a, the nitrogen adsorption–desorption isotherms of CH and CH/TU demonstrated standard type IV characteristics with hysteresis loops, as classified by the IUPAC system [28]. These isotherms exhibited a distinct pore condensation step at relative pressures (P/P$_0$) between 0.63 and 1.21, representing the existence of mesoporous structures with a tight mesopore size distribution. Furthermore, the marked rise in nitrogen absorption above a relative pressure (P/P$_0$) of 0.99 and the steady increase below the P/P$_0$ of 0.45 suggested that the structures of both samples included both macropores and micropores. According to the pore size distribution shown in Figure 2b, the pore sizes are estimated to be approximately 4.00 and 4.60 nm for CH and CH/TU, respectively. The BET specific surface areas of CH and CH/TU were 1292.63 m^2 g^{-1} and 2124.78 m^2 g^{-1}, respectively. Following carbonization, highly porous amorphous carbon products were obtained from the Hanji-based raw materials. Such numerical information is summarized in Table 1. The XRD spectra of all samples (Figure 2c) displayed two distinct diffraction peaks at around 24° and 43°, which align with the (002) and (100) crystal planes of graphite within a hexagonal crystal structure, respectively [29]. This finding indicates the amorphous

nature of carbon materials, confirming that the CH and CH/TU samples were in an amorphous carbon form. Figure 2d illustrates the Raman spectra of CH and CH/TU, both exhibiting two characteristic peaks at approximately 1340 and 1585 cm^{-1}, which correspond to the D- and G-bands, respectively. The D-band was primarily related to the out-of-plane A_{1g} vibration, indicative of structural defects, edge defects, and dangling sp^3 bonds in amorphous carbon [30]. Moreover, the breathing vibration of a ring consisting of six carbon atoms was accountable for the abovementioned finding. In contrast, the G-band was attributed to the in-plane vibration mode of the E_{2g} of sp^2 carbon (graphite-like carbon) [31]. Comparatively, the intensity of the D-band of CH/TU was greater, which confirms a high degree of amorphous carbon morphology, consistent with the XRD analysis. To ensure an accurate comparison of the structural properties of the carbon materials, the integrated peak areas of the D- and G-bands were quantified from the Raman spectra. This method allows for a more comprehensive evaluation of the total contributions of the D- and G-bands, providing a robust analysis of the structural disorder and sp^2 carbon content. The I_D/I_G ratio, calculated using the integrated areas, was found to be 1.17 for CH and 1.32 for CH/TU. The higher I_D/I_G ratio for CH/TU indicates a greater degree of structural disorder compared to CH, which can be ascribed to the incorporation of heteroatoms or the formation of vacancies during the synthesis process.

Figure 2. (**a**) Nitrogen adsorption−desorption curves, (**b**) pore size dispersion profile, (**c**) X−ray diffraction (XRD) patterns, and (**d**) Raman spectra of CH and CH/TU samples.
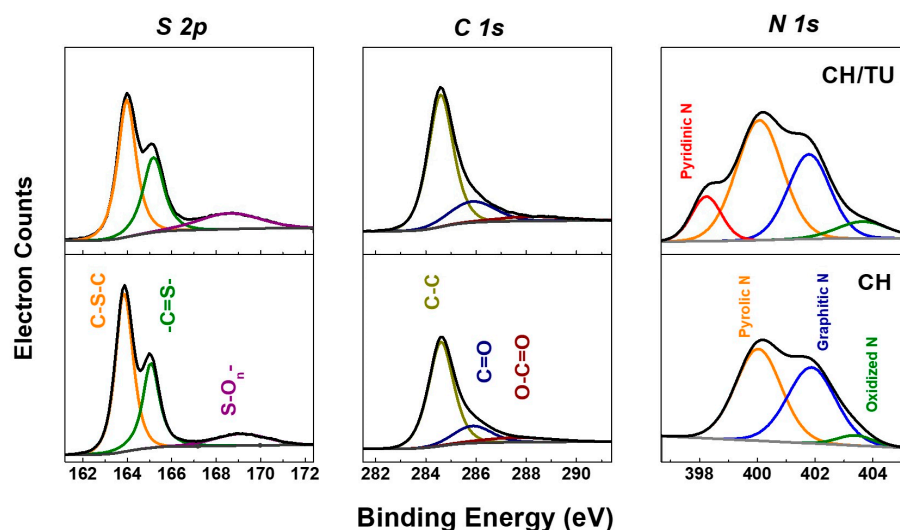
Table 1. BET analysis results for CH and CH/TU samples.

Carbon	CH	CH/TU
Surface Area, [1] [m^2 g^{-1}]	1292.6350	2124.7841
Total Pore Volume, [2] [cm^3 g^{-1}]	0.63920	1.21402
Pore Diameter, [3] [nm]	40,068	4.6078

[1] Brunauer−Emmett−Teller surface area; [2] total pore volume at P/P$_0$ = 0.010040578; [3] average Barrett−Joyner−Halenda adsorption pore diameter.

In Figure 3, the surface chemical compositions of CH and CH/TU are analyzed using XPS. The S 2p, C 1s, and N 1s binding energies for both samples were examined to evaluate the chemical bonds and elemental forms in each sample. The S 2p spectrum revealed S bonding, exhibiting peaks corresponding to C–S–C (163.9 eV), C=S (165.1 eV), and S–O$_n^-$ (168.6 eV) bonds. Compared with CH, CH/TU contained S in more diverse chemical forms, indicating the presence of diverse surface-active sites, which could enhance its potential for energy storage applications. A deconvolution of the C 1s spectrum revealed three primary peaks: C–C bonds (284.7 eV), C=O bonds (287.7 eV), and O–C=O bonds (289.7 eV). The C–C bond is a characteristic of graphitic carbon and contributes to its increased electrical conductivity [32]. The C=O and O–C=O bonds suggest the existence of oxygenated functional groups on the surface, which could enhance hydrophilicity and provide active sites. The N 1s spectra revealed a peak at approximately 398.5 eV, corresponding to pyridinic N in CH/TU, which could serve as a catalytic active site and improve reactivity. In addition, the CH/TU sample exhibited higher intensities of pyrrolic N and graphitic N peaks than CH, suggesting enhanced structural stability and conductivity. The elemental ratios determined by XPS analysis based on the integrated peak areas of CH and CH/TU samples are presented in Table 2. For CH, the respective values for C 1s, S 2p, and N 1s are 70.69, 17.1, and 1.57 atomic %, while CH/TU shows 61.59, 21.12, and 2.62 atomic %. Comparative XPS analysis indicated that CH/TU contained higher amounts of N and S compounds than CH, suggesting greater reactivity in its electrochemical reactions. In particular, the S bonding states in the S 2p spectrum showed diverse chemical forms, providing a variety of surface-active sites that could improve the functionality of Li–S batteries. The N bonding states indicated that N doping enhanced conductivity and stability [33]. Therefore, the functional properties of CH/TU make it suitable for enhancing electrochemical performance, indicating its potential suitability for advanced energy storage applications.
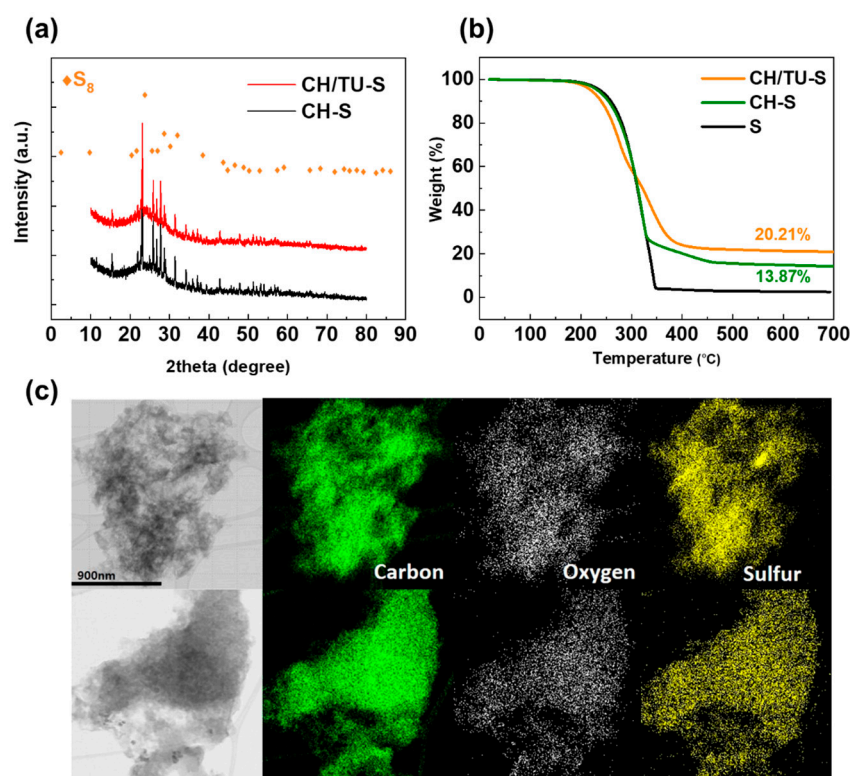

Figure 3. High-resolution X-ray photoelectron spectrometry spectra of S 2p, C 1s, and N 1s for CH and CH/TU samples.

XRD analysis was conducted to compare the structural characteristics of the bonds with S in the two samples, CH and CH/TU-S (Figure 4a). The S$_8$ pattern at the top represents the peak positions of crystalline S, serving as a reference for comparison based on the crystal S structure. The XRD patterns revealed the structural differences between CH-S and CH/TU-S. CH/TU-S exhibited stronger peaks than CH-S, suggesting higher crystallinity. However, the Full Width at Half Maximum (FWHM) values provided addi-

tional insights into the structural characteristics of the samples. The FWHM for the most prominent peak of CH-S was calculated to be 0.1707, while that of CH/TU-S was 0.2757. The strong peaks observed in the 20–30° region for CH/TU-S further support the presence of specific crystalline structures and composite formations resulting from interactions with S. This unique combination of a high peak intensity and a broader FWHM suggests that CH/TU-S strikes a balance between structural order and amorphous characteristics, making it a promising candidate for lithium–sulfur batteries. The ability to combine active surface sites with structural stability provides CH/TU-S with the potential for enhanced electrochemical performance.

Table 2. Elemental ratio determined through XPS analysis based on integrated peak areas of CH and CH/TU samples.

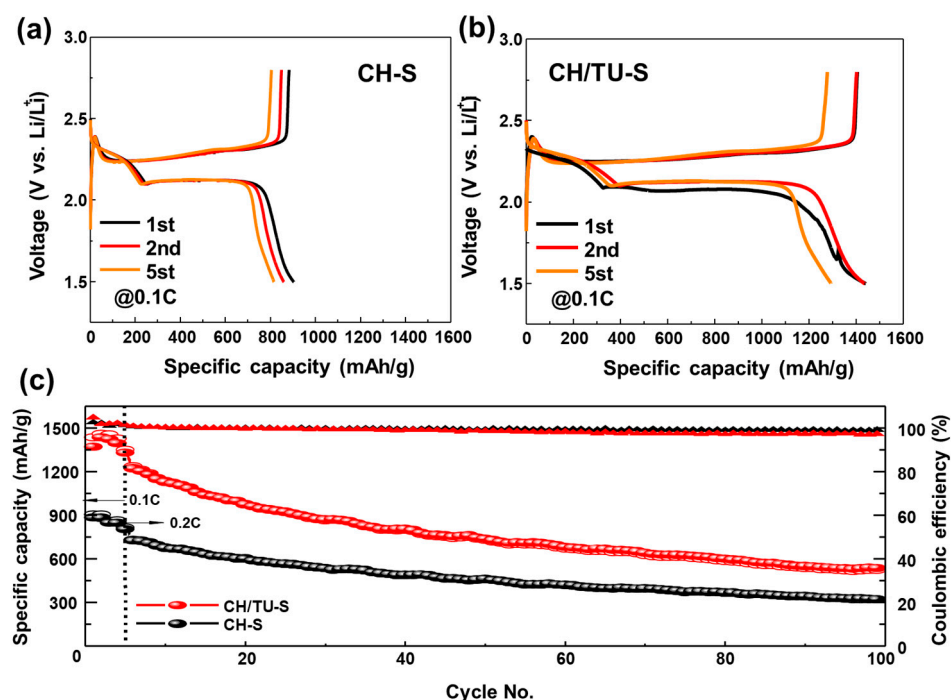| Samples	Atomic %			
	C 1s	S 2p	N 1s	O 1s
CH	70.69	17.1	1.57	10.63
CH/TU	61.59	21.12	2.62	14.66

Figure 4. (**a**) XRD patterns, (**b**) thermogravimetric analysis results for S content evaluation, and (**c**) transmission electron microscopy images and energy-dispersive X-ray spectroscopy maps of C, O, and S in CH-S and CH/TU-S samples.

As illustrated in Figure 4b, the weight change rate with temperature is analyzed using TG analysis. The graph demonstrates that the sample weight decreases with an increase in temperature. The CH-S sample began to lose weight at approximately 200 °C, which was similar to the CH/TU-S sample. Consequently, 13.78% residue of CH-S was obtained, whereas 20.21% residue of CH/TU-S was obtained, highlighting the difference in the thermal decomposition residue of S. The significantly higher residues of CH-S and CH/TU-S compared to pure S indicates the presence of thermally stable components other than S. In addition, the higher residue of CH/TU-S leaves compared to CH-S suggests a

relatively higher thermal stability for CH/TU-S, as more material remains after thermal decomposition. The TEM images and energy-dispersive X-ray spectroscopy maps of CH-S and CH/TU-S are illustrated in Figure 4c. The mapping of S, C, and O indicates the compositions of CH-S and CH/TU-S. The mapping indicates the uniform distribution of S throughout the synthesized composites, providing functional characteristics such as the suppression of dissolution during the charge–discharge processes [34].

Figure 5a,b illustrate the first charge–discharge profiles at 0.1 C, comparing the electrochemical properties of CH-S and CH/TU-S. The initial discharge capacities of CH-S and CH/TU-S were 903 and 1065 mAh/g, respectively, with that of CH/TU-S being closer to the theoretical capacity of S. However, the discharge capacity of CH-S decreased rapidly after the second and fifth cycles, indicating challenges in capacity retention owing to the loss of S, polysulfide shuttle effects, or inefficiencies in the electrode structure [1].

Figure 5. Electrochemical charging–discharging profiles of Li-S cells at 0.1 C for the 1st, 2nd, and 5th cycles of (**a**) CH-S and (**b**) CH/TU-S. (**c**) Cycling stability and coulombic efficiency of Li-S cells.
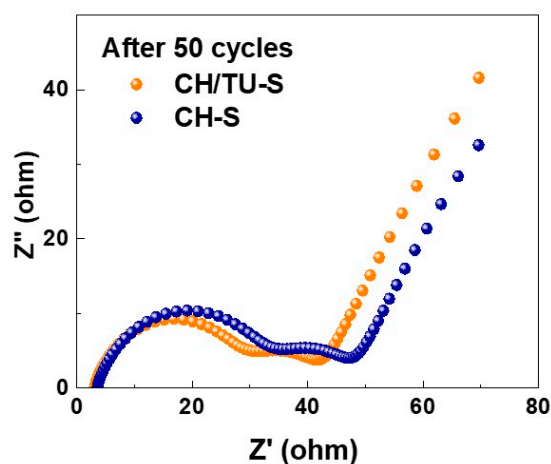
In contrast, CH/TU-S exhibited minimal capacity fading and superior capacity retention, suggesting that the dissolution and migration of polysulfides were effectively suppressed and highlighting the stability of the electrode structure. Notably, CH-S exhibited shorter and less-stable flat voltage plateaus than CH/TU-S. In CH/TU-S, flat plateaus were better maintained, indicating greater voltage stability. Voltage stability was analyzed based on the changes in the flat voltage plateaus during cycling. The flat plateau of CH/TU-S decreased by approximately 0.05 V over the cycles, whereas CH-S exhibited a larger decrease of approximately 0.2 V. The markedly reduced voltage fluctuation of CH/TU-S demonstrated its enhanced voltage stability in comparison to CH-S. This development could be ascribed to the uniform dispersion of S and suppression of the polysulfide shuttle effect. In addition, CH/TU-S retained a relatively high capacity even after the fifth cycle, demonstrating stability during the charge–discharge processes. This improved performance could be attributed to the uniform encapsulation of S and the contribution of the conductive carbon matrix. CH/TU-S exhibited superior capacity retention, voltage stability, and cycling stability compared to CH-S, making it more suitable for high-performance

Li-S battery applications. The electrode structure of CH/TU-S effectively suppressed polysulfide dissolution and enhanced electrochemical stability.

Figure 5c compares the cycling durability and coulombic performances of CH-S and CH/TU-S over 100 cycles. The first specific capacity of CH-S at 0.1 C was approximately 903 mAh/g. However, after 100 cycles, the capacity decreased significantly to approximately 200 mAh/g. This rapid decline indicates various issues, such as low S utilization, polysulfide shuttle effects, and the structural degradation of the electrode. In contrast, CH/TU-S had a higher initial specific capacity of approximately 1065 mAh/g at 0.1 C, outperforming CH-S. Even after 100 cycles, the CH/TU-S sample maintained a high capacity of approximately 600 mAh/g, demonstrating a significantly improved cycling stability. This relatively slowly fading capacity suggests that S encapsulation was effectively achieved, suppressing polysulfide dissolution and shuttle effects. Moreover, CH/TU-S maintained nearly 100% coulombic efficiency throughout the cycling process, indicating minimal active material loss during the charge–discharge cycles. These results validate the effectiveness of CH/TU-S in mitigating polysulfide re-deposition and enhancing electrochemical stability.

The electrochemical properties of the CH-S and CH/TU-S composites were assessed through EIS after 50 cycles, as shown in Figure 6. After 50 cycles, the EIS spectra of both samples displayed two compressed semicircles, followed by an extended slanted line. The starting point in the high-frequency region represents the solution resistance (R_s); lower R_s values indicate superior ionic conductivity. As Shown in Table 3, the R_s values of CH-S and CH/TU-S were 3.36 and 2.90 Ω, respectively, indicating that CH/TU-S exhibited superior ionic conductivity in the electrolyte.

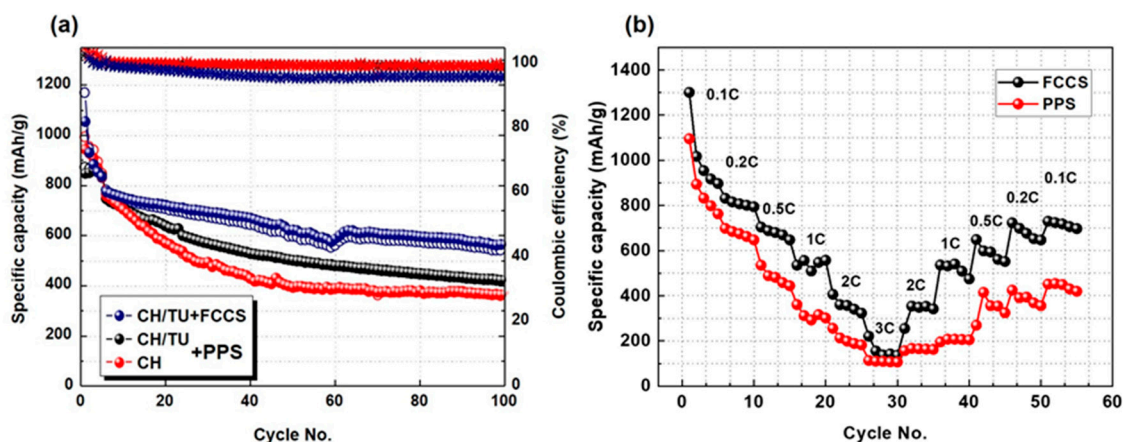**Figure 6.** Electrochemical impedance profiles of Li-S batteries measured after 50 cycles at 0.2 C.

Table 3. Values of R_s and R_{ct} for CH-S and CH/TU-S cells after 50 cycles.

	R_s (Ω)	R_{ct} (Ω)
CH-S	3.36	44.575
CH/TU-S	2.90	38.754

The charge-transfer resistance (R_{ct}) observed in the mid-frequency region represents the interfacial R_{ct}. CH/TU-S exhibited a smaller semicircle diameter than CH-S, indicating improved charge transfer at the interface between the electrode and electrolyte. The R_{ct} values were 44.575 Ω for CH-S and 38.754 Ω for CH/TU-S. The lower R_{ct} of CH/TU-S indicated superior electrochemical reactivity at the electrode surface and reduced R_{ct}. This finding could be attributed to a more uniform S distribution on the electrode surface or to a reduced level of irreversible Li polysulfide deposition. The slope in the low-frequency

range (Warburg impedance) reflected resistance to Li ion diffusion [9]. CH/TU-S exhibited a steeper slope than CH-S, suggesting lower Li ion diffusion resistance and faster ion transport. The EIS analysis confirmed that CH/TU-S had a more optimized electrode structure, indicating its potential for superior Li-S battery performance.

To enhance the performance of Li-S cells further, a flake carbon-coated separator (FCCS) was fabricated and incorporated into the cell [35]. Figure 7a illustrates the specific capacity changes in the cells with and without FCCSs over 100 cycles, highlighting a comparison between the FCCS and a conventional polypropylene separator (PPS). The CH/TU-S+FCCS sample presented a first specific capacity of 1300 mAh/g, outperforming the other samples, highlighting that the use of a FCCS significantly improved S utilization within the cell. Even after 100 cycles, the CH/TU-S+FCCS sample maintained a high specific capacity of approximately 620 mAh/g, demonstrating superior cycling stability compared with the other samples. The FCCS effectively suppressed the polysulfide shuttle effect and aided in stabilizing S on the electrode surface, minimizing S loss during cycling. In contrast, the CH/TU-S+PPS sample had an initial specific capacity of approximately 993 mAh/g, which was lower than that of the FCCS-incorporated cell. Following 100 cycles, the capacity decreased to approximately 420 mAh/g, indicating a lower capacity retention than that of the FCCS sample. This result indicated that the conventional PPS failed to adequately suppress the polysulfide shuttle effect. The CH-S+PPS sample exhibited the lowest performance, with its capacity decreasing to approximately 366 mAh/g after 100 cycles. Among the three samples, it exhibited the lowest cycling stability. This finding could be attributed to its low S utilization, its inadequate suppression of the polysulfide shuttle effect, and the structural degradation of the electrode.

Figure 7. (**a**) Cycling performance of CH/TU and CH coupled with flake carbon-coated separator (FCCS) or polypropylene separator (PPS), and (**b**) rate capability of CH/TU sample applied with FCCS and PPS.

Figure 7b relates the specific capacity changes in the cells using a PPS at varying charge–discharge rates. The FCCS cell exhibited an initial specific capacity of approximately 1171 mAh/g, which significantly exceeded that of the PPS cell (872 mAh/g). This finding indicates that the FCCS maximized S utilization and provided higher electrochemical activity in the initial charging and discharging cycles. In contrast, the relatively low capacity of the PPS cell suggests its inability to effectively suppress the polysulfide shuttle effect or achieve uniform S dispersion. In the FCCS cell, as the charge–discharge rate increased from 0.1 to 3 C, the specific capacity decreased; however, it remained above approximately 200 mAh/g at 3 C. When the rate was 0.1 C, the specific capacity reached 730 mAh/g. This finding demonstrates that the FCCS cell maintained a relatively stable performance even at high charge–discharge rates, reflecting its superior structural stability

and electrochemical efficiency. In contrast, the PPS cell showed a rapid decrease in capacity with increasing charge–discharge rates, dropping below 110 mAh/g at 3 C. When the rate was reduced, the capacity recovery was limited, reaching 450 mAh/g. This result indicates that the PPS was less effective in mitigating the polysulfide shuttle effect and lacked the electrochemical stability required for high-rate cycling. The FCCS cell also demonstrated high-capacity retention over more than 50 cycles, maintaining stable performance despite changes in the charge–discharge rates. This finding could be attributed to the ability of FCCSs to effectively suppress polysulfide dissolution and migration while supporting S immobilization, minimizing the active material loss. In contrast, the PPS cell exhibited relatively poor cycling stability with pronounced performance degradation under varying charge–discharge rates, highlighting the limitations of PPS for S immobilization and polysulfide shuttle suppression.

In conclusion, the FCCS cell demonstrated a superior initial capacity, a remarkable recovery capability under varying charge–discharge rates, and excellent cycling stability. These are critical characteristics for high-performance Li-S battery applications. Conversely, the PPS cell exhibited a lower initial capacity, significant performance deterioration at high charge–discharge rates, and a limited recovery capability, resulting in a substantial performance gap compared with the FCCS cell.

4. Conclusions

In this research, the performance of Li-S batteries was effectively improved using Hanji-based carbon materials. Due to its porous structure and high surface area, Hanji demonstrated excellent electrical conductivity and structural stability. These characteristics addressed the critical challenges of Li-S batteries, such as the polysulfide shuttle effect and active material loss, providing a viable solution to these issues. These results highlight the potential of Hanji-based carbon as a material for next-generation Li-S batteries, offering high performance and long-term durability. In particular, FCCSs exhibited superior electrochemical stability and recovery capabilities compared with PPSs, demonstrating their effectiveness in suppressing the polysulfide shuttle effect in Li-S batteries. This result highlights the considerable potential of a FCCS to improve both the performance and longevity of Li-S batteries. Based on these findings, further design optimization can significantly improve the commercial viability of Hanji-based carbon resources for high-performance Li-S batteries.

Author Contributions: Experiments, data result analysis, writing—original draft, and writing, Y.C.; data result analysis and methodology, J.L., J.-P.K. and S.-J.L.; material synthesis and conceptualization, E.D.J.; conceptualization and editing, J.-S.B.; supervision, data curation, and editing, H.-C.S. All authors have read and agreed to the published version of the manuscript.

Data Availability Statement: The data presented in this study are available on request from the corresponding author.

Conflicts of Interest: The authors declare no competing financial interests or personal relationships that could influence the work reported in this study.

References

1. Zhang, S.S. Liquid electrolyte lithium/sulfur battery: Fundamental chemistry, problems, and solutions. *J. Power Sources* **2013**, *231*, 153–162. [CrossRef]
2. Mikhaylik, Y.V.; Akridge, J.R. Polysulfide shuttle study in the Li/S battery system. *J. Electrochem. Soc.* **2004**, *151*, A1969–A1976. [CrossRef]

3.　Seh, Z.W.; Sun, Y.; Zhang, Q.; Cui, Y. Designing high-energy lithium–sulfur batteries. *J. Mater. Chem. A* **2019**, *7*, 2942–2964. [CrossRef] [PubMed]

4.　Dong, C.; Gao, W.; Jin, B.; Jiang, Q. Advances in Cathode Materials for High-Performance Lithium-Sulfur Batteries. *iScience* **2018**, *6*, 151–198. [CrossRef]

5.　Wang, M.; Xia, X.; Zhong, Y.; Wu, J.; Xu, R.; Yao, Z.; Tu, J. Porous Carbon Hosts for Lithium–Sulfur Batteries. *Chem. Eur. J.* **2019**, *25*, 3710–3725. [CrossRef]

6.　Zhang, Q.; Cheng, X.B.; Huang, J.Q.; Peng, H.J.; Wei, F. Review of Carbon Materials for Advanced Lithium–Sulfur Batteries. *Carbon* **2015**, *81*, 850. [CrossRef]

7.　Sahore, R.; Levin, B.D.; Pan, M.; Muller, D.A.; DiSalvo, F.J.; Giannelis, E.P. Design Principles for Optimum Performance of Porous Carbons in Lithium–Sulfur Batteries. *Adv. Energy Mater.* **2016**, *6*, 1600134. [CrossRef]

8.　Song, M.-K.; Cairns, E.J.; Zhang, Y. Lithium/sulfur batteries with high specific energy: Old challenges and new opportunities. *Nanoscale* **2013**, *5*, 2186–2204. [CrossRef]

9.　Manthiram, A.; Fu, Y.; Chung, S.-H.; Zu, C.; Su, Y.-S. Rechargeable lithium–sulfur batteries. *Chem. Rev.* **2014**, *114*, 11751–11787. [CrossRef]

10.　Raza, H.; Bai, S.; Cheng, J.; Majumder, S.; Zhu, H.; Liu, Q.; Zheng, G.; Li, X.; Chen, G. Li-S batteries: Challenges, achievements, and opportunities. *Electrochem. Energy Rev.* **2023**, *6*, 29. [CrossRef]

11.　Shahryari, Z.; Yeganeh, M.; Gheisari, K.; Ramezanzadeh, B. A brief review of the graphene oxide-based polymer nanocomposite coatings: Preparation, Characterization, and properties. *J. Coat. Technol. Res.* **2021**, *18*, 945–969. [CrossRef]

12.　Agobi, A.U.; Idowu, M.A.; Ezugwu, C.K.; Githinji, G.M.; Oyeniran, K. A review on conducting polymers-based composites for energy storage application. *J. Chem. Rev.* **2019**, *1*, 19–34. [CrossRef]

13.　Jeon, T.; Lee, Y.C.; Hwang, J.Y.; Choi, B.C.; Lee, S.; Jung, S.C. Strong lithium-polysulfide anchoring effect of amorphous carbon for lithium–sulfur batteries. *Curr. Appl. Phys.* **2021**, *22*, 94–103. [CrossRef]

14.　Spahr, M.E.; Goers, D.; Leone, A.; Stallone, S.; Grivei, E. Development of carbon conductive additives for advanced lithium-ion batteries. *J. Power Sources* **2011**, *196*, 3404–3413. [CrossRef]

15.　Fu, A.; Wang, C.; Pei, F.; Cui, J.; Fang, X.; Zheng, N. Recent advances in hollow porous carbon materials for lithium–sulfur batteries. *Small* **2019**, *15*, e1804786. [CrossRef] [PubMed]

16.　Liu, M.; Deng, N.; Ju, J.; Fan, L.; Wang, L.; Li, Z.; Zhao, H.; Yang, G.; Kang, W.; Yan, J.; et al. A review: Electrospun nanofiber materials for lithium-sulfur batteries. *Adv. Funct. Mater.* **2019**, *29*, 1905467. [CrossRef]

17.　Chen, X.; Zhang, Y.; Liu, T.; Li, H.; Cheng, J.; Zhou, T.; Zheng, Y.; Zhang, Q.; Huang, J.; Wang, Y. Polysulfide Filter and Dendrite Inhibitor: Highly Graphitized Wood Framework Inhibits Polysulfide Shuttle and Lithium Dendrites in Li–S Batteries. *Adv. Funct. Mater.* **2021**, *31*, 2102458. [CrossRef]

18.　Wang, F.; Liao, T.; Hu, S.; Du, J.; Cai, Y.; Jiang, J.; Li, Q. Effects of Binder Content on Potato Starch-Derived Porous Carbon Microspheres for High-Performance Supercapacitors. *J. Energy Storage.* **2024**, *91*, 112081. [CrossRef]

19.　Zhao, S.; Li, C.; Wang, W.; Zhang, H.; Gao, M.; Xiong, X.; Wang, A.; Yuan, K.; Huang, Y.; Wang, F. A novel porous nanocomposite of sulfur/carbon obtained from fish scales for lithium-sulfur batteries. *J. Mater. Chem. A* **2013**, *1*, 3334–3339. [CrossRef]

20.　Yan, Y.; Wei, Y.; Li, Q.; Shi, M.; Zhao, C.; Chen, L.; Xu, Y. Activated Porous Carbon Materials with Ultrahigh Specific Surface Area Derived from Banana Peels for High-Performance Lithium–Sulfur Batteries. *J. Mater. Sci. Mater. Electron.* **2018**, *29*, 11325–11335. [CrossRef]

21.　Gu, X.; Wang, Y.; Lai, C.; Qiu, J.; Li, S.; Hou, Y.; Martens, W.; Mahmood, N.; Zhang, S. Microporous bamboo biochar for lithium-sulfur batteries. *Nano Res.* **2015**, *8*, 129–139. [CrossRef]

22.　Ren, G.; Li, S.; Fan, Z.X.; Warzywoda, J.; Fan, Z. Soybean-Derived Hierarchical Porous Carbon with Large Sulfur Loading and Sulfur Content for High-Performance Lithium–Sulfur Batteries. *J. Mater. Chem. A.* **2016**, *4*, 16507–16515. [CrossRef]

23.　Guo, J.; Zhang, J.; Jiang, F.; Zhao, S.; Su, Q.; Du, G. Microporous Carbon Nanosheets Derived from Corncobs for Lithium–Sulfur Batteries. *Electrochim. Acta.* **2015**, *176*, 853–860. [CrossRef]

24.　Ma, Z.; Sui, W.; Liu, J.; Wang, W.; Li, S.; Chen, T.; Yang, G.; Zhu, K.; Li, Z. Pomelo Peel-Derived Porous Carbon as Excellent LiPS Anchor in Lithium-Sulfur Batteries. *J. Solid State Electrochem.* **2022**, *26*, 973–984. [CrossRef]

25.　Lu, S.; Chen, Y.; Zhou, J.; Wang, Z.; Wu, X.; Gu, J.; Jiang, L. A Sheet-Like Carbon Matrix Hosted Sulfur as Cathode for High-Performance Lithium-Sulfur Batteries. *Sci. Rep.* **2016**, *6*, 20445. [CrossRef] [PubMed]

26.　Choi, Y.; Lee, S.Y.; Bae, J.S.; Lee, S.J.; Kim, H.K.; Jeong, E.D.; Shin, H.C. Nitrogen and sulfur co-doped porous carbon derived from thiourea and calcium citrate for lithium–sulfur batteries. *Appl. Sci.* **2020**, *10*, 1263. [CrossRef]

27.　Lee, S.Y.; Choi, Y.; Kim, J.K.; Lee, S.J.; Bae, J.S.; Jeong, E.D. Biomass-garlic-peel-derived porous carbon framework as a sulfur host for lithium-sulfur batteries. *J. Ind. Eng. Chem.* **2021**, *94*, 272–281. [CrossRef]

28.　Thommes, M.; Kaneko, K.; Neimark, A.V.; Olivier, J.P.; Rodriguez-Reinoso, F.; Rouquerol, J.; Sing, K.S.W. Physisorption of gases, with special reference to the evaluation of surface area and pore size distribution (IUPAC Technical Report) [IUPAC technical report]. *Pure Appl. Chem.* **2015**, *87*, 1051–1069. [CrossRef]

29. Zhao, X.; Hayner, C.M.; Kung, M.C.; Kung, H.H. Flexible holey graphene paper electrodes with enhanced rate capability for energy storage applications. *ACS Nano* **2011**, *5*, 8739–8749. [CrossRef] [PubMed]

30. Kumar, S.T.S.; Kumar, B.S.; Balaji, S.; Sanjeeviraja, C.; Selvan, R.K. Preparation of activated carbon from sorghum pith and its structural and electrochemical properties. *Mater. Res. Bull.* **2011**, *46*, 413–418. [CrossRef]

31. Robertson, J. Hard amorphous (diamond-like) carbons. *Prog. Solid State Chem.* **1991**, *21*, 199–333. [CrossRef]

32. Gengenbach, T.R.; Major, G.H.; Linford, M.R.; Easton, C.D. Practical Guides for X-ray photoelectron spectroscopy (XPS): Interpreting the Carbon 1s Spectrum. *J. Vac. Sci. Technol. A* **2021**, *39*, 013204. [CrossRef]

33. Artyushkova, K.; Kiefer, B.; Halevi, B.; Knop-Gericke, A.; Schlögl, R.; Atanassov, P. Density functional theory calculations of XPS binding energy shift for nitrogen-containing graphene-like structures. *Chem. Commun.* **2013**, *49*, 2539–2541. [CrossRef] [PubMed]

34. Bharathkumar, H.J.; Shivankar, B.R.; Krishnamurty, S.; Chen, D.; Caruso, R.A.; Krishnamoorthy, K. Polyvalent interaction and confinement to suppress polysulfide dissolution and improve electrocatalysis. *Catal. Sci. Technol.* **2024**, *14*, 3416–3423. [CrossRef]

35. He, J.; Gao, Z.; Li, X. Yeast-derived carbon nanotube-coated separator for high performance lithium-sulfur batteries. *JOM* **2021**, *73*, 2516–2524. [CrossRef]